

University of Wollongong

Research Online

Australian Institute for Innovative Materials -
Papers

Australian Institute for Innovative Materials

1-1-2020

Improved Na storage and Coulombic efficiency in TiP2O7@C microflowers for sodium ion batteries

Jun Pan

Nana Wang

University of Wollongong, nanaw@uow.edu.au

Lili Li

Feng Zhang

Zhenjie Cheng

See next page for additional authors

Follow this and additional works at: <https://ro.uow.edu.au/aiimpapers>



Part of the [Engineering Commons](#), and the [Physical Sciences and Mathematics Commons](#)

Recommended Citation

Pan, Jun; Wang, Nana; Li, Lili; Zhang, Feng; Cheng, Zhenjie; Li, Yanlu; Yang, Jian; and Qian, Yitai, "Improved Na storage and Coulombic efficiency in TiP2O7@C microflowers for sodium ion batteries" (2020).

Australian Institute for Innovative Materials - Papers. 4321.

<https://ro.uow.edu.au/aiimpapers/4321>

Research Online is the open access institutional repository for the University of Wollongong. For further information contact the UOW Library: research-pubs@uow.edu.au

Improved Na storage and Coulombic efficiency in TiP2O7@C microflowers for sodium ion batteries

Abstract

© 2020, Tsinghua University Press and Springer-Verlag GmbH Germany, part of Springer Nature. Ti-based anode materials in sodium ion batteries have attracted extensive interests due to its abundant resources, low toxicity, easy synthesis and long cycle life. However, low Coulombic efficiency and limited specific capacity affect their applications. Here, cubic-phase TiP2O7 is examined as anode materials, using in-situ/ex-situ characterization techniques. It is concluded that the redox reactions of Ti⁴⁺/Ti³⁺ and Ti³⁺/Ti⁰ consecutively occur during the discharge/charge processes, both of which are highly reversible. These reactions make the specific capacity of TiP2O7 even higher than the case of TiO₂ that only contains a simple anion, O²⁻. Interestingly, Ti species participate only one of the redox reactions, due to the remarkable difference in local structures related to the sodiation process. The stable discharge/charge products in TiP2O7 reduce the side reactions and improve the Coulombic efficiency as compared to TiO₂. These features make it a promising Ti-based anode for sodium ion batteries. Therefore, TiP2O7@C microflowers exhibit excellent electrochemical performances, ~ 109 mAh·g⁻¹ after 10,000 cycles at 2 A·g⁻¹, or 95.2 mAh·g⁻¹ at 10 A·g⁻¹. The results demonstrate new opportunities for advanced Ti-based anodes in sodium ion batteries. [Figure not available: see fulltext.]

Disciplines

Engineering | Physical Sciences and Mathematics

Publication Details

Pan, J., Wang, N., Li, L., Zhang, F., Cheng, Z., Li, Y., Yang, J. & Qian, Y. (2020). Improved Na storage and Coulombic efficiency in TiP2O7@C microflowers for sodium ion batteries. *Nano Research*,

Authors

Jun Pan, Nana Wang, Lili Li, Feng Zhang, Zhenjie Cheng, Yanlu Li, Jian Yang, and Yitai Qian

TABLE OF CONTENTS

Improved Na Storage and Coulombic Efficiency in TiP_2O_7 @C Microflowers for Sodium Ion Batteries

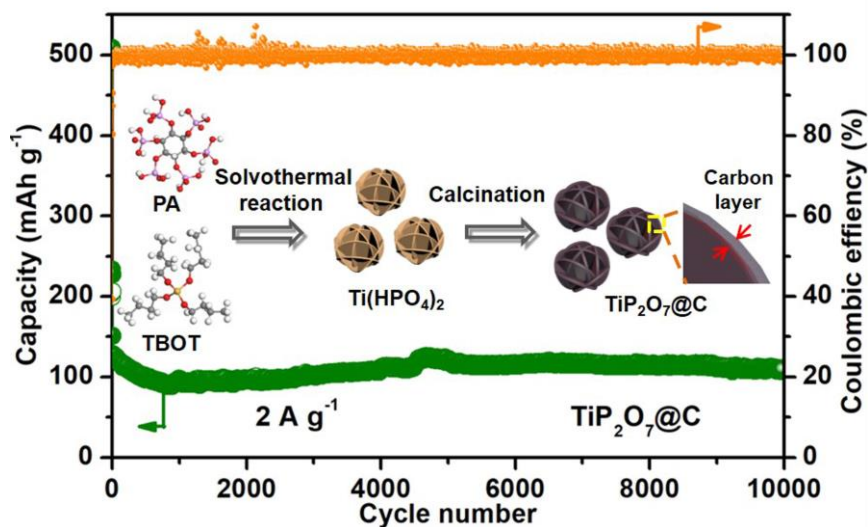
Jun Pan^{1,2}, Nana Wang³, Lili Li⁴, Feng Zhang¹, Zhenjie Cheng¹, Yanlu Li³, Jian Yang,^{*1,2} and Yitai Qian¹

¹ Key Laboratory of Colloid and Interface Chemistry, Ministry of Education, School of Chemistry and Chemical Engineering Shandong University, Jinan 250100, P. R. China.

² Shenzhen Research Institute of Shandong University, Shenzhen 518000, P. R. China.

³ Institute for Superconducting and Electronic Materials, Australian Institute for Innovative Materials, University of Wollongong Innovation Campus, North Wollongong New South Wales 2500, Australia.

⁴ State Key Lab of Crystal Materials, Shandong University, Jinan 250100, P. R. China.



TiP_2O_7 as a promising Ti-based anode material, combines enhanced specific capacity, increased coulombic efficiency and low operation voltage together. These features can be associated with the underlying electrochemical reactions for Na storage, very different from the case of TiO_2 .

Improved Na Storage and Coulombic Efficiency in $\text{TiP}_2\text{O}_7@\text{C}$ Microflowers for Sodium Ion Batteries

Jun Pan^{1,2}, Nana Wang³, Lili Li⁴, Feng Zhang¹, Zhenjie Cheng¹, Yanlu Li⁴, Jian Yang,^{*1,2} (✉) and Yitai Qian¹

¹ Key Laboratory of Colloid and Interface Chemistry, Ministry of Education, School of Chemistry and Chemical Engineering Shandong University, Jinan 250100, P. R. China.

² Shenzhen Research Institute of Shandong University, Shenzhen 518000, P. R. China.

³ Institute for Superconducting and Electronic Materials, Australian Institute for Innovative Materials, University of Wollongong Innovation Campus, North Wollongong New South Wales 2500, Australia.

⁴ State Key Lab of Crystal Materials, Shandong University, Jinan 250100, P. R. China.

Received: day month year

Revised: day month year

Accepted: day month year
(automatically inserted by
the publisher)

© Tsinghua University
Press and Springer-Verlag
Berlin Heidelberg 2014

KEYWORDS

TiP_2O_7 ,
electrochemical reactions,
anodes,
sodium ion batteries

ABSTRACT

Ti-based anode materials in sodium ion batteries have attracted extensive interests due to its abundant resources, low toxicity, easy synthesis and long cycle life. However, low coulombic efficiency and limited specific capacity affect their applications. Here, cubic-phase TiP_2O_7 is examined as anode materials, using *in-situ/ex-situ* characterization techniques. It is concluded that the redox reactions of $\text{Ti}^{4+}/\text{Ti}^{3+}$ and $\text{Ti}^{3+}/\text{Ti}^0$ consecutively occur during the discharge/charge processes, both of which are highly reversible. These reactions make the specific capacity of TiP_2O_7 even higher than the case of TiO_2 that only contains a simple anion, O^{2-} . Interestingly, Ti species participate only one of the redox reactions, due to the remarkable difference in local structures related to the sodiation process. The stable discharge/charge products in TiP_2O_7 reduce the side reactions and improve the coulombic efficiency as compared to TiO_2 . These features make it a promising Ti-based anode for sodium ion batteries. Therefore, $\text{TiP}_2\text{O}_7@\text{C}$ microflowers exhibit excellent electrochemical performances, $\sim 109 \text{ mAh g}^{-1}$ after 10000 cycles at 2 A g^{-1} , or 95.2 mAh g^{-1} at 10 A g^{-1} . The results demonstrate new opportunities for advanced Ti-based anodes in sodium ion batteries.

1 Introduction

Na-ion batteries (NIBs) as one of next-generation batteries attract extensive attention in the past years, due to the abundant reserves of Na in earth, the similar working principles and fabrication protocols to those of Li-ion batteries (LIBs), as well as the low-cost current collector for anodes [1,2]. However, the relatively large ionic radius and heavy ionic mass

of Na^+ impede its diffusion in electrodes, greatly increasing the voltage hysteresis and reducing the round-trip energy efficiency [3,4]. Meanwhile, the large ionic radius of Na^+ also induces a giant volume change in the discharge/charge processes, easily leading to structure collapse and particle pulverization. Then, the effective electrical connection between active materials and current collectors is lost, resulting in a rapid decay of performances [5,6]. To

Address correspondence to yangjian@sdu.edu.cn.

address these issues, the selection of electrode materials is very important, because the electrode materials based on intercalation reactions always exhibit the small volume changes in theory [7-18]. In this case, they can exhibit excellent cycle lives, such as hard carbon, TiO_2 , and so on. Different from hard carbon, TiO_2 works in a moderate voltage range of 0.2-1.5 V, thus avoiding the formation of Na dendrites upon cycling. Meanwhile, TiO_2 is nontoxic, easy to be prepared and stable at ambient conditions. Thus, TiO_2 has been regarded as one of promising anode materials of NIBs in the past years [19-22]. However, the specific capacity of TiO_2 is quite limited. More worse, it shows the poor coulombic efficiency, especially for the first several cycles.

To solve the problems, understanding the electrochemical reactions of TiO_2 is necessary. Unfortunately, only a few works investigated these reactions in details [23-26]. The classic work came from Passerini's group [23], who reported the formation of metallic Ti (Ti^0) and Ti^{3+} in the discharge process on the basis of X-ray photoelectron spectroscopy (XPS). They thought that 1) the reduction from Ti^{4+} to Ti^0 was fully irreversible; and 2) NaO_2 was produced along with the continuous evolution of oxygen in the discharging process. So, it is believed that the former reduces the initial coulombic efficiency and the specific capacity. The latter induces the severe safety issues. Inspired by our recent works [27,28], if the simple anion, O^{2-} , is replaced by polyanions like phosphates, the formation of the unstable discharged products like NaO_2 can be avoided, thus reducing the side reactions and increasing the coulombic efficiency. Meanwhile, the bulky polyanions expand the crystal lattice and increase the open space for Na-ion transportation, facilitating the electrochemical reactions. More interestingly, the polyanions might increase the electrochemical activity of Ti^0 , enabling the oxidation of Ti^0 back to Ti^{3+} or Ti^{4+} . This possibility is supported by the recent report about SbVO_4 [29], where VO_4^{3-} promoted the redox reaction of $\text{Sb}^{3+}/\text{Sb}^0$ in LIBs/NIBs. Finally, there are still many polyanions that have been not explored before or seldom studied. Therefore, it is believed that this work opens a door for the future design of advanced electrode materials. So far, there are only a few works using TiP_2O_7 as electrode materials for LIBs/NIBs [30-34]. The majority of them focused on its performances in

aqueous electrolytes. Palacin and Chen reported that the Na storage in cubic-phase TiP_2O_7 was almost negligible ($\sim 20 \text{ mAh g}^{-1}$) within 1.0-3.5 V (vs. Na^+/Na) [30,31]. Li and Wu synthesized oxygen vacancy-enriched TiP_2O_7 as an anode material of NIBs and potassium-ion batteries (PIBs) [32]. However, this " TiP_2O_7 " is more likely to be the composite of TiO_2 (major phase)/ TiP_2O_7 (minor phase), in view of X-ray diffraction (XRD) patterns, P contents, and thermogravimetric (TG) analysis. So, the electrochemical properties of TiP_2O_7 for Na storage are still unclear yet.

Here, the electrochemical reactions of cubic-phase TiP_2O_7 for Na storage are investigated by *in-situ* XRD patterns, *ex-situ* high-resolution transmission electron microscope (HRTEM) images, selected-area electron diffraction (SAED) patterns and XPS spectra. The redox reactions of $\text{Ti}^{4+}/\text{Ti}^{3+}$ and $\text{Ti}^{3+}/\text{Ti}^0$ consecutively occur during the discharge/charge processes. Different from the case of TiO_2 , the redox reaction of $\text{Ti}^{3+}/\text{Ti}^0$ is also highly reversible, which makes the specific capacity of TiP_2O_7 superior to that of TiO_2 even if there is a heavy "dead" mass of $\text{P}_2\text{O}_7^{4-}$. More interestingly, Ti species participate only one of the redox reactions, either $\text{Ti}^{4+}/\text{Ti}^{3+}$ or $\text{Ti}^{3+}/\text{Ti}^0$. To our knowledge, it is first time to disclose the electrochemical reactions of TiP_2O_7 in NIBs. Similar to the case of $\text{NaTi}_2(\text{PO}_4)_3$, the coulombic efficiency of TiP_2O_7 is improved upon cycling over TiO_2 , due to the stable discharge/charge products and the reduced side reactions. Thus, TiP_2O_7 combines the high coulombic efficiency of $\text{NaTi}_2(\text{PO}_4)_3$ and the low operation voltage of TiO_2 together, in addition to the enhanced capacity. These features make TiP_2O_7 a promising Ti-based anode material for NIBs. As a result, $\text{TiP}_2\text{O}_7/\text{C}$ microflowers deliver a capacity of 109 mAh g^{-1} after 10000 cycles at 2 A g^{-1} , or 95.2 mAh g^{-1} at 10 A g^{-1} .

2 Experimental

2.1 Materials synthesis

Synthesis of TiO_2 : TiO_2 was synthesized by a reported method [35]. Firstly, 1.0 mL of TiCl_3 (15.0-20.0% in 30% HCl, Aladdin) was mixed with 30 mL of ethylene glycol (EG, 99%, Sinopharm) and 3 mL of deionized water. After this solution was stirred for 15 minutes, it was transferred to a Teflon-lined stainless-

steel autoclave with a capacity of 60 mL. The autoclave was then kept at 150 °C for 12 h. The product was collected by centrifugation, washed with deionized water and anhydrous ethanol, and dried at 60 °C in vacuum overnight. Finally, the white powders were annealed at 600 °C in air for 4 h.

Synthesis of TiP_2O_7 and $\text{TiP}_2\text{O}_7\text{@C}$: The synthesis was similar to that of TiO_2 [36]. Firstly, 0.5 mL of tetrabutyl titanate (TBOT) (98%, Sinopharm) was dropped into 40 mL of anhydrous ethanol (99.7%, Sinopharm). After sonication for 30 minutes, 0.4 mL of phytic acid (PA) ($\geq 70\%$, Sinopharm) was added slowly with vigorous stirring. Then, the solution was transferred to a Teflon-lined stainless-steel autoclave with a capacity of 60 mL. After 12 h at 200 °C, the product was collected by centrifugation, washed with deionized water and anhydrous ethanol, and dried at 60 °C in vacuum overnight. Finally, TiP_2O_7 or $\text{TiP}_2\text{O}_7\text{@C}$ was obtained by annealing the powders at 800 °C for 4 h in air or in N_2 , respectively.

Synthesis of $\text{NaTi}_2(\text{PO}_4)_3$: $\text{NaTi}_2(\text{PO}_4)_3$ was synthesized by a reported method [37]. Firstly, 0.68 mL of TBOT was dropped into 20 mL of ethylene glycol (EG, 99%, Sinopharm). After 5 minutes, 20 mL of 0.05 M $\text{NaH}_2\text{PO}_4 \cdot 2\text{H}_2\text{O}$ (99%, Sinopharm) and 0.125 mL of H_3PO_4 (99%, Sinopharm) were added slowly with vigorous stirring. The obtained solution was transferred to a Teflon-lined stainless-steel autoclave with a capacity of 60 mL. Then, the autoclave was kept at 180 °C for 12 h. The product was collected by centrifugation, washed by deionized water and anhydrous ethanol, and dried at 60 °C in vacuum overnight. Finally, the powders were annealed at 700 °C in air for 4 h.

2.2 Materials characterization

XRD patterns were obtained on an X-ray diffractometer (Bruker D8 Advanced, $\text{Cu } \alpha$ radiation, $\lambda = 1.5418 \text{ \AA}$, Germany). Scanning electron microscope (SEM) images were acquired by a field-emission scanning electron microscope (Zeiss Gemini 300, Germany). Transmission electron microscope (TEM) images, HRTEM images, X-ray energy-dispersive spectrum (EDS) spectra, high-angle annular dark-field scanning TEM (HAADF-STEM) images and element maps were recorded using an aberration-corrected TEM microscope (FEI Tecnai F20, USA).

XPS was achieved on an X-ray photoelectron spectrometer (ESCALAB 250, Thermo Scientific, USA). Raman spectra were taken on a micro-Raman spectrometer (HORIBA JY Lab RAM HD88, Japan), using an excitation of 632 nm at room temperature. N_2 sorption isotherms were measured on a sorption analyzer (Micromeritics ASAP 2020 HD88, USA) at 77 K. TG analysis was acquired from a thermal analyzer (Mettler Toledo TGA/SDTA 851, Switzerland) from room temperature to 800 °C in air.

In-situ XRD chamber was similar to that reported in literature [38]. Specifically, the working electrode, electrolyte-saturated separator, and Na foil were stacked together in specially-designed cells, where the cell case attached to the working electrode was holed and sealed by a Be window to allow X-ray pass and reflect. The galvanostatic discharge/charge of the cells was conducted at a current density of 25 mA g^{-1} . Each XRD pattern was acquired in a step incremental of 0.02° between $2\theta = 10^\circ$ and 80° at a scanning rate of $0.08^\circ \text{ s}^{-1}$. At least 50 scans were performed during a full discharge/charge cycle.

2.3 Electrochemical measurements

Electrochemical performances of TiO_2 , TiP_2O_7 , $\text{NaTi}_2(\text{PO}_4)_3$ and $\text{TiP}_2\text{O}_7\text{@C}$ as anode materials for NIBs were tested in CR2032-type coin cells. As the active materials, TiO_2 , TiP_2O_7 , $\text{NaTi}_2(\text{PO}_4)_3$ or $\text{TiP}_2\text{O}_7\text{@C}$ was mixed with acetylene black and sodium alginate (SA) in a weight ratio of 7:2:1 with droplets of deionized water. Then, the mixture was manually ground, resulting in a homogeneous slurry. The slurry was spread on a clean copper foil by a doctor blade. After dried at 60 °C in vacuum for 12 h, the foil was pouched into small discs with a diameter of ~12 mm. The mass loading of active materials on the discs was about 1-1.5 mg cm^{-2} . Next, the discs as the working electrode were assembled in an Ar-filled glove box (Mikrouna, Super 1220/ 750/900, $\text{H}_2\text{O} < 1 \text{ ppm}$; $\text{O}_2 < 1 \text{ ppm}$) with sodium metal as the counter electrode, glass fiber (Whatman GF/F) as a separator, and 1.0 M NaClO_4 in propylene carbonate (PC) containing 3 wt% fluoroethylene carbonate (FEC) as the electrolyte. The specific capacity also included the mass of carbon in the case of $\text{TiP}_2\text{O}_7\text{@C}$. Cyclic voltammetry (CV) curves were measured on an electrochemical workstation (CHI 760E, China) at

room temperature. Electrochemical impedance spectra (EIS) were obtained from an electrochemical workstation (Auto-lab PGSTAT 302N, Switzerland) in a frequency range of 100 KHz to 0.01 Hz.

3 Results and discussion

TiP₂O₇@C microflowers were synthesized *via* a solvothermal reaction of PA and TBOT, followed by a high-temperature calcination (Fig. 1(a)). The solvothermal reaction produced Ti(HPO₄)₂ microflowers with organic species adsorbed on the surface (Fig. S1 in Electronic Supplementary Material (ESM)) that then decomposed at a high temperature, leading to TiP₂O₇@C in N₂ or TiP₂O₇ in air. Fig. 1(b) shows the XRD pattern of as-obtained product, where all the diffraction peaks can be attributed to cubic-phase TiP₂O₇ (JCPDS Card, No. 38-1468). But the diffraction peaks of carbon are absent in the pattern, probably due to the limited content and poor crystallinity of carbon. In order to clarify the existence of carbon in the product, Raman spectrum, TG curve and XPS were recorded. In the Raman spectrum, the two

characteristic peaks of carbon, D band at 1330 cm⁻¹ and G band at 1610 cm⁻¹ [38], are clearly identified (Fig. 1(c)), confirming the presence of carbon in the product. The small but visible peak at 1050 cm⁻¹ that originates from the stretching vibration of PO₄ [39], is related to TiP₂O₇ in the product. Compared to the case of carbon, the small intensity of this peak can be assigned to the core-shell structure of TiP₂O₇@C, in which the Raman scattering of PO₄ is heavily shielded by carbon. TG curve of the product in air displays a sharp weight loss of ~16.9 wt% between 550-600 °C (Fig. 1(d)), likely resulted from the removal of carbon in TiP₂O₇@C. The high-resolution spectrum of C 1s indicates there are multiple carbon species in TiP₂O₇@C (Fig. 1(e)), *i.e.* C=C at 284.6 eV, C-C at 285.2 eV, C-O at 286.4 eV, and O-C=O at 289.7 eV [40]. These oxygenous groups facilitate the tight contact between carbon and TiP₂O₇, reducing the charge-transfer resistances during the sodiation/desodiation processes. Meanwhile, the valence states of Ti and P are also checked by XPS. The high-resolution spectrum of Ti 2p consist of two peaks at 459.5 eV and 465.5 eV (Fig. 1(f)), well consistent with

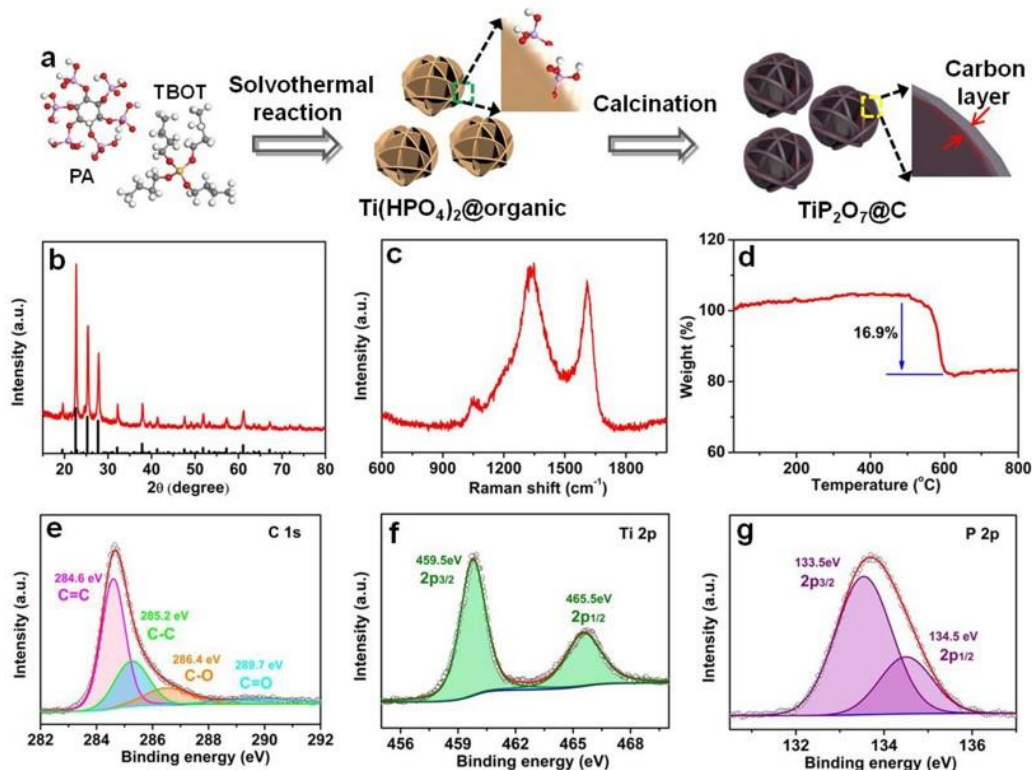


Fig. 1 Chemical synthesis and structure characterization of TiP₂O₇@C. (a) Synthesis process of TiP₂O₇@C, (b) XRD pattern, (c) Raman spectrum, (d) TGA curve, XPS spectra of C 1s (e), Ti 2p (f), P 2p (g).

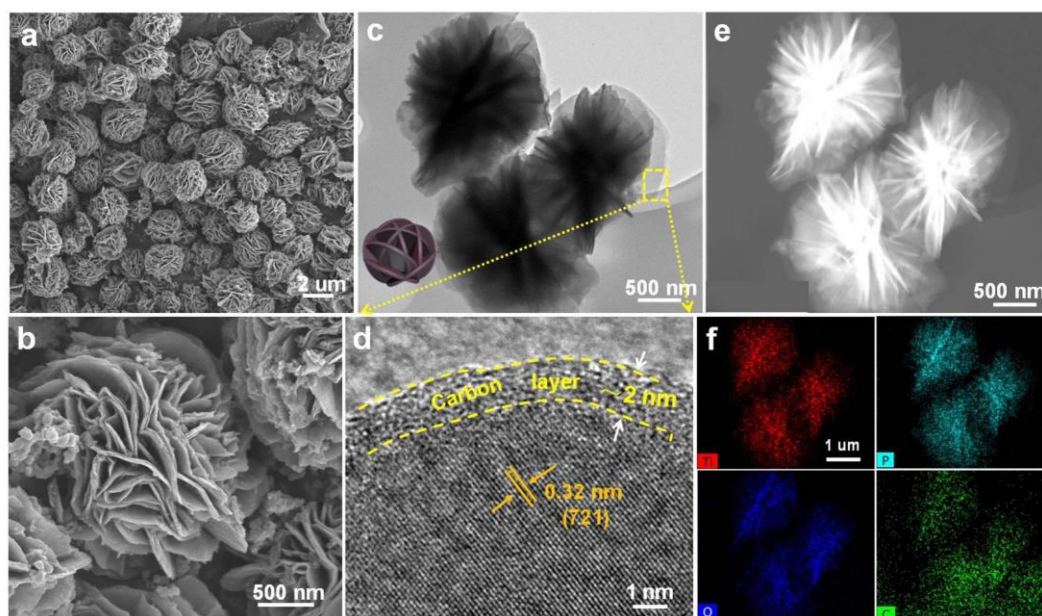


Fig. 2 Morphology characterization of $\text{TiP}_2\text{O}_7@\text{C}$. (a, b) FESEM images, (c) TEM image, (d) HRTEM image, (e) HAADF-STEM image and (f) elemental maps of Ti, P, O, and C.

Ti $2p_{3/2}$ and Ti $2p_{1/2}$ of Ti^{4+} [41]. The high-resolution XPS spectrum of P 2p presents an asymmetric peak that is then fitted into two peaks at 133.5 eV and 134.5 eV (Fig. 1(g)). These data are in good accordance with the reported data of P $2p_{3/2}$ and P $2p_{1/2}$ from $\text{P}_2\text{O}_7^{4-}$ [42]. The molar ratio of Ti/P is $\sim 1:1.94$, close to the chemical stoichiometry of TiP_2O_7 . The similar result is observed in EDS (Fig. S2).

$\text{TiP}_2\text{O}_7@\text{C}$ basically inherits the unique flower-like structure of $\text{Ti}(\text{HPO}_4)_2$, as confirmed by SEM images. As presented in Fig. 2a, these flower-like micro-particles have a uniform size and a high yield. The average diameter of these microflowers is approximately $\sim 2 \mu\text{m}$. The close check on a single microflower reveals that it is composed of interconnected petals with a thickness of $\sim 56 \text{ nm}$ (Fig. 2b). The petals are randomly curved, leaving plenty of voids between them. This structure feature will promote the electrolyte penetration and accommodate the volume change upon cycling, thereby improving reaction kinetics and structure stability. The similar conclusions are also obtained by TEM image (Fig. 2c). HRTEM image on the petal edge of a microflower shows the clear lattice fringes with an interlayer spacing about 0.32 nm (Fig. 2d) that can be assigned to (721) planes of cubic-phase TiP_2O_7 [31]. The formation of TiP_2O_7 is also supported by SAED

pattern (Fig. S3). On the other hand, it is noted that these lattice fringes do not propagate throughout the particle, but become discontinuous at the edge, a typical scenario of amorphous materials. Associated this result with XRD, Raman, XPS and synthesis process, it is concluded that the amorphous shell must be carbon. Thereby, the product could be identified as $\text{TiP}_2\text{O}_7@\text{C}$ microflowers in a core-shell structure. Fig. 2e and 2f show high-angle annular dark-field scanning TEM (HAADF-STEM) image and element maps of Ti, P, O and C, where the distribution patterns of Ti, P, O and C are in good agreement with the proposed structure. In spite of the open structure, $\text{TiP}_2\text{O}_7@\text{C}$ microflowers only present a specific surface area of $\sim 24.3 \text{ m}^2 \text{ g}^{-1}$ (Fig. S4), due to the large particle size.

Then, the electrochemical measurements were conducted on $\text{TiP}_2\text{O}_7@\text{C}$. First of all, TiP_2O_7 is compared to the well-known Ti-based oxides, TiO_2 and $\text{NaTi}_2(\text{PO}_4)_3$ to understand the possible features. The selection of the two oxides as the references is due to the following reasons. Firstly, Ti species in TiO_2 , TiP_2O_7 and $\text{NaTi}_2(\text{PO}_4)_3$ is Ti^{4+} . Secondly, although these oxides have different structures, Ti species exist in the same term, TiO_6 . Thirdly, the electrochemical activity in these oxides comes from Ti species, not other elements. Finally, Na-storage

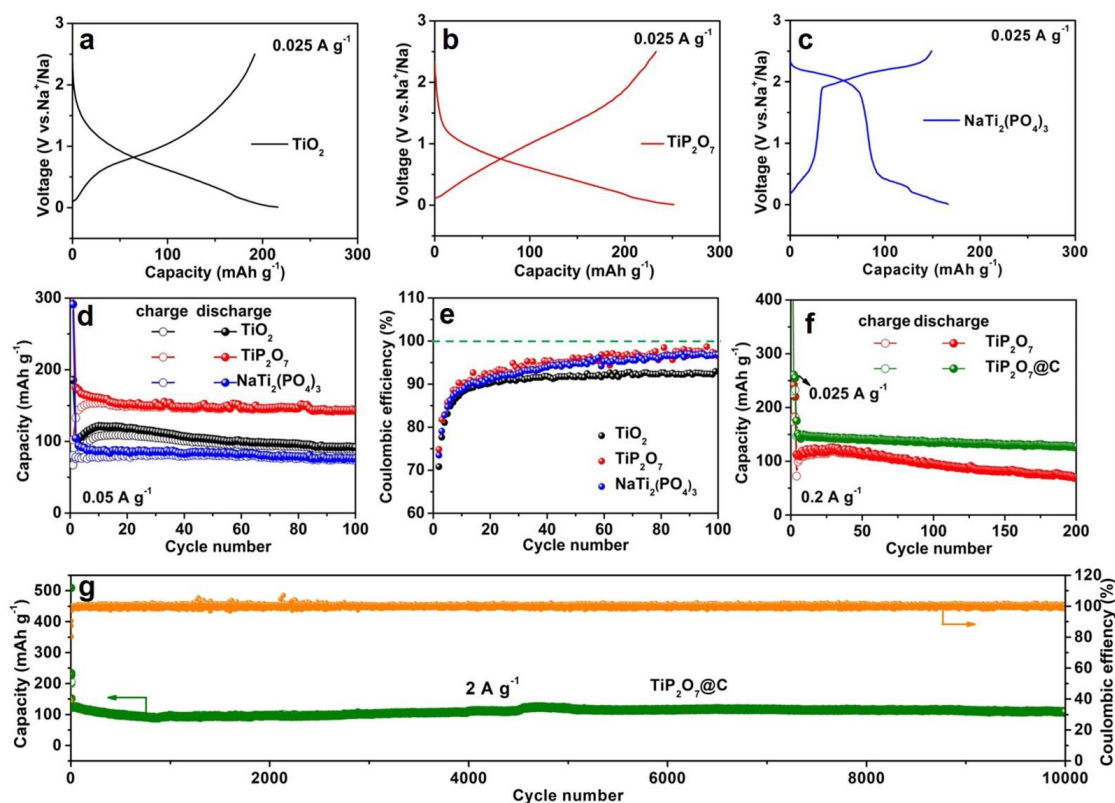


Fig. 3 Electrochemical properties of TiP₂O₇, TiP₂O₇@C and Ti-based oxides for Na storage. (a-c) Discharge/charge voltage profiles of TiO₂, TiP₂O₇ and NaTi₂(PO₄)₃ at the third cycle. (d) Cycling performances and (e) Coulombic efficiency of TiO₂, TiP₂O₇ and NaTi₂(PO₄)₃ at 0.05 A g⁻¹. (f) Cycling performances of TiP₂O₇ and TiP₂O₇@C at 0.2 A g⁻¹. (g) Long-term cycling performance of TiP₂O₇@C at 2 A g⁻¹.

properties of TiO₂ and NaTi₂(PO₄)₃ have been well-documented in literature [43–46]. The XRD patterns and SEM images of home-made TiO₂ and NaTi₂(PO₄)₃ are shown in Fig. S5–S7, where both of them consist of layered-like nanostructures in similar sizes. The working electrodes based on TiO₂, TiP₂O₇ and NaTi₂(PO₄)₃ were obtained by the same protocol to eliminate the artificial effect caused by cell fabrication. The electrochemical performances were measured at a small current density (~25 mA g⁻¹) to minimize the size/shape effect as much as possible. Fig. 3a–3c represent the galvanostatic discharge/charge profiles of TiO₂, TiP₂O₇ and NaTi₂(PO₄)₃ as anode materials for NIBs at the third cycle. It is believed that the data at the third cycle can effectively alleviate the effect of side reactions on the voltage profiles that is always serious at the first two cycles (Fig. S8). As a result, TiP₂O₇ exhibits a specific capacity (~255 mAh g⁻¹), a moderate operation

voltage (~0.97 V) and a high coulombic efficiency (~95.3%), combining the low operation voltage of TiO₂ and the high coulombic efficiency of NaTi₂(PO₄)₃ together. Meanwhile, the increased specific capacity of TiP₂O₇ over TiO₂ is surprising, because the “dead” mass of P₂O₇⁴⁻ is thought to be much larger than that of O²⁻ in TiO₂. This improvement is even more pronounced in terms of Na number stored per formula (Fig. S9). It can be ascribed to the enhanced reversible reaction between Ti³⁺ and Ti⁰ in TiP₂O₇, as discussed later. The advantage in coulombic efficiency is also noted (TiP₂O₇ ~95.3% vs. TiO₂ ~92.5%). The low coulombic efficiency will consume the limited electrolytes and Na ions offered by cathode materials, leading to severe capacity degradation.

To verify if the above advantages persist upon cycling, the cycling performances were measured at a small current density of 50 mA g⁻¹ (Fig. 3d). TiP₂O₇

delivers a specific capacity of $\sim 144 \text{ mAh g}^{-1}$ after 100 cycles, higher than those of TiO_2 (92.1 mAh g^{-1}) and $\text{NaTi}_2(\text{PO}_4)_3$ (76.5 mAh g^{-1}). It should be pointed out that all the materials are tested in carbonate-based electrolyte without carbon coating. Beside the high capacity, the superior coulombic efficiency of TiP_2O_7 also remains in the repeated cycles (Fig. 3e). It can be attributed to the stable discharge/charge products related to $\text{P}_2\text{O}_7^{4-}$ that effectively reduce the side reactions and improve the coulombic efficiency. This advantage is also observed in the case of $\text{NaTi}_2(\text{PO}_4)_3$, confirming the benefit from polyanions. Despite it is just a small difference, it can cause serious consequences after hundreds of cycles. Using TiO_2 vs. TiP_2O_7 as an example, the average coulombic efficiency of TiP_2O_7 over 100 cycles at 0.05 A g^{-1} is $\sim 97.4\%$, higher than $\sim 92.3\%$ of TiO_2 (Fig. 3e). But the cumulative coulombic efficiency decreases to 4.53% for TiP_2O_7 or to 0.045% for TiO_2 , indicating that most of the cathode material will be deactivated if they are directly used for full cells. In spite of this, the case of TiP_2O_7 is still two orders higher than the data of TiO_2 . The cycling performances of TiP_2O_7 at a high rate are evaluated at 0.2 A g^{-1} . Before that, the electrode was electrochemically activated at 0.025 A g^{-1} for the first three cycles. As displayed in Fig. 3f, the capacity of TiP_2O_7 sustains at $\sim 120 \text{ mAh g}^{-1}$ before 30 cycles and then gradually decays to $\sim 70 \text{ mAh g}^{-1}$ after 200 cycles,

58.3% of the capacity after the electrochemical activation. Since this capacity degradation can be inhibited by carbon coating, $\text{TiP}_2\text{O}_7@\text{C}$ presents a capacity of $\sim 128 \text{ mAh g}^{-1}$ and the capacity retention of $\sim 86.9\%$ after the same cycles. Even after 10000 cycles at a current density of 2 A g^{-1} , there is still a reversible capacity of 109 mA h g^{-1} (Fig. 3g). Such a long cycle life is comparable to the best results of TiO_2 (Tab. S1). The discharge/charge profiles and morphology of $\text{TiP}_2\text{O}_7@\text{C}$ is roughly kept after 10000 cycles (Fig. S10), although its surface is covered by a thick solid-electrolyte-interphase (SEI) film.

Fig. 4a and 4b give the rate performances of TiP_2O_7 and $\text{TiP}_2\text{O}_7@\text{C}$. In the range from 0.1 A g^{-1} to 10 A g^{-1} , $\text{TiP}_2\text{O}_7@\text{C}$ shows the higher capacity over TiP_2O_7 . Even at a current density of 10 A g^{-1} , it still reverses a capacity of $\sim 95.2 \text{ mAh g}^{-1}$. As the current density returns to 0.1 A g^{-1} , the capacity goes back to 214.7 mAh g^{-1} , indicating the good durability to the high rates. These results indicate that carbon coating effectively improves the electrochemical kinetics, also supported by EIS and CV curves. The Nyquist plots of the fully-discharged electrodes, no matter what are active materials (TiP_2O_7 or $\text{TiP}_2\text{O}_7@\text{C}$), consist of one depressed semicircle in the region of high-to-medium frequencies, followed by a diffusion drift in the region of low frequencies (Fig. S11). Then, the ohmic resistance (R_s), the surface-film resistance (R_i) and the

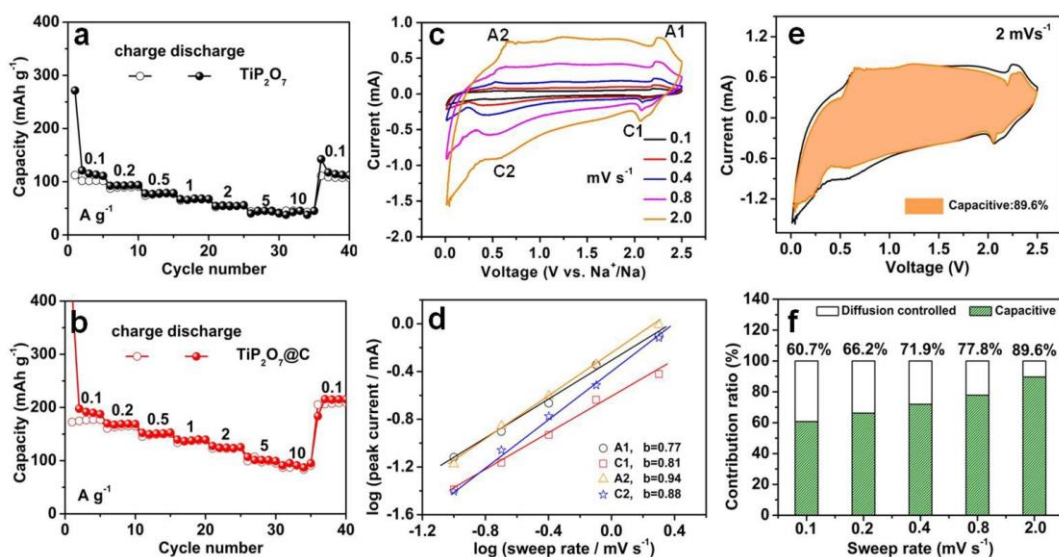


Fig. 4 Electrochemical kinetics of $\text{TiP}_2\text{O}_7@\text{C}$ during sodiation/desodiation. (a, b) Rate performances of TiP_2O_7 and $\text{TiP}_2\text{O}_7@\text{C}$. (c) CV curves of $\text{TiP}_2\text{O}_7@\text{C}$ at various scan rates, (d) Plots of \log (peak current) versus \log (sweep rate), (e) Contribution of capacitive behavior to Na storage in CV curves at 2 mV s^{-1} , (f) Contribution ratio of capacitive behavior at different sweep rates.

charge-transfer resistance (R_{ct}), are derived by equivalent circuits. As listed in Tab. S2, the electrode made of $TiP_2O_7@C$ exhibits much smaller R_f and R_{ct} than those of TiP_2O_7 . The smaller resistances facilitate the charge transportation and promote the electrochemical kinetics in the discharge process. The superior reaction kinetics is also supported by CV curves at different sweep rates [47]. As shown in Fig. 4c, CV curves basically keep the similar contour as the sweep rate increases. The logarithmic plot of the peak current (i_p) versus sweep rate (v) is indicative of the rate-limited characteristics in the term of b . In our case, b values of the cathodic/anodic peaks are 0.81/0.77 and 0.88/0.94 (Fig. 4d), indicating the mixed contribution of a diffusion-controlled process ($b=0.5$) and a surface-controlled process ($b=1.0$). The capacity contributions from the surface-controlled process and the diffusion-controlled process can be roughly estimated, as detailed in many reports [48]. It is noted that the surface-controlled process contributes 89.6% of the overall capacity of $TiP_2O_7@C$ at 2 mV s^{-1} (Fig. 4e). This data steady decreases from 89.6% to 60.7% as the sweep rate is reduced to 0.1 mV s^{-1} (Fig. 4f).

TiP_2O_7 , instead of $TiP_2O_7@C$, was used to clarify the underlying electrochemical reactions for Na storage. As illustrated in Fig. 5a, TiP_2O_7 exhibits a reversible capacity of $\sim 255\text{ mAh g}^{-1}$ for Na storage,

demonstrating its good electrochemical activity to Na^+/Na . Then, *in-situ* XRD patterns of the electrode using TiP_2O_7 as the active material (Fig. 5b) were detected to reveal the evolution of crystal structures during the first two cycles. It is noted that the diffraction peaks of TiP_2O_7 at 22.6° , 25.3° and 27.7° slightly shift to the low angles, as the electrode is discharged to 0.5 V. Such a shift corresponds to the lattice expansion, indicating that a small amount of Na ions has been intercalated into TiP_2O_7 . Despite Na-ion intercalation definitely induces structure stress, the crystal structure still remains at this stage. The continuous discharge of the electrode to 0.22 V makes the diffraction peaks broad and weak, suggesting that the crystal structure is severely distorted. At the end of the discharge process (0.01 V), these diffraction peaks completely vanish from the XRD pattern, probably due to the poor crystallinity and small sizes of the discharged products. The amorphous feature of the electrode remains in the charge process and in the following cycle. This result, *i.e.* the crystal structure won't be recovered again in the charge process, is a typical feature of anode materials involving conversion reactions. Therefore, it is believed that the sodiation/desodiation processes of TiP_2O_7 may involve certain conversion reactions.

Advanced TEM techniques and XPS spectrum are taken to identify the products in the discharge/charge

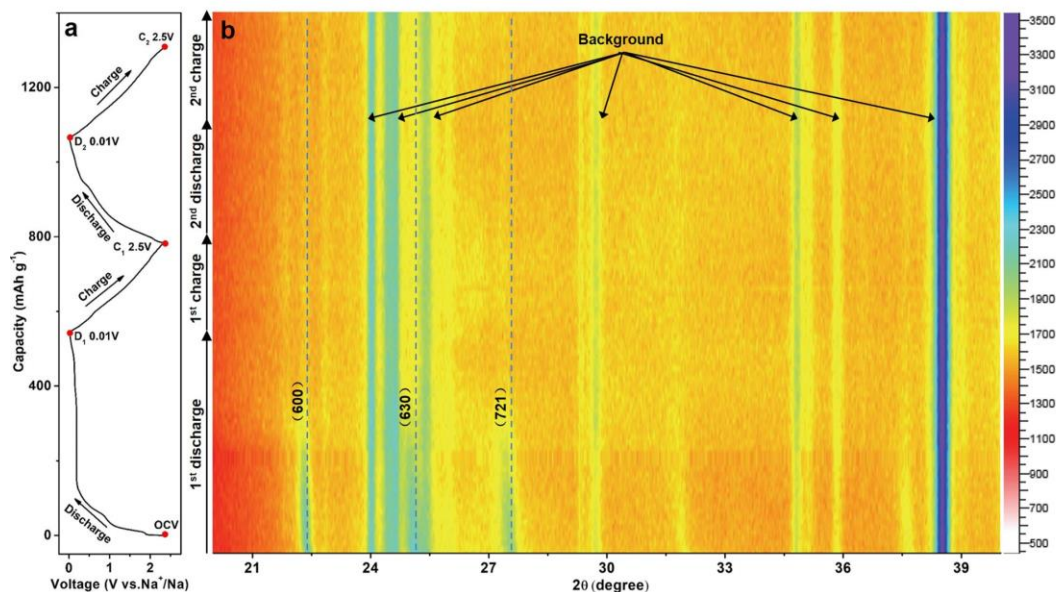


Fig. 5 In-situ XRD patterns of the electrode based on TiP_2O_7 in the first two cycles. (a) Discharge/charge voltage profiles, and (b) In-situ XRD patterns.

processes. Fig. 6a shows the HRTEM image of the fully-discharged electrode, where the straight lattice fringes with the interlayer spacings of 0.33 nm and 0.23 nm are clearly observed. They can be correlated to the crystal planes of $\text{Na}_4\text{P}_2\text{O}_7$ (004) and Ti (110) respectively. The existences of metallic Ti (Ti^0) and $\text{Na}_4\text{P}_2\text{O}_7$ in the fully-discharged electrode suggest the conversion reactions in the discharge process. The similar result is also obtained by the SAED pattern (Fig. 6b). When the electrode is charged back to 2.5 V, only a few HRTEM images and SAED patterns present the lattice fringes and diffraction spots of TiP_2O_7 (Fig. 6d and 6e). The electrode materials are basically amorphous. So, XPS was measured to gain more insights about the components in these electrodes. As displayed in Fig. S12, the binding energy of P 2p in the fully-discharged/charged electrodes is almost the same, excluding that there are redox reactions on the P species during the cycles. In the high-resolution spectrum of O 1s, three binding energies, which belongs to M-O/P-O (~531.1 eV), C-O/O-H (~532.9 eV), and Na Auger (~536.4 eV), are observed for the fully-discharged/charged electrodes (Fig. S13). The intensities of Na Auger and C-O/O-H in the fully-charged electrode decrease relative to that of M-O/P-O, which can be ascribed to the electrochemical desodiation, and/or the decomposition of surface films. The further distinguishing of different oxygen species is very difficult, in view of various oxygen-containing species in the electrodes, such as M/P-O, polymer binder, SEI film, residual electrolytes, and so on. Therefore, the useful information from the O 1s spectra is limited. So, the following discussion has to focus on Ti 2p. Fig. 6c presents the high-resolution spectrum of Ti $2p_{3/2}$ in the fully-discharged electrode, where the two peaks at 453.1 eV and 457.7 eV can be attributed to Ti^0 and Ti^{3+} . Compared to the case in TiP_2O_7 (Fig. 1f), the result confirms again that there is a reducing reaction on Ti species during the discharge process. Based on the peak areas, the contents of Ti^{3+} and Ti^0 are roughly estimated as 69.8% and 30.2% (Fig. 6c). The high content of Ti^{3+} in the electrode indicates the limited reduction from Ti^{3+} to Ti^0 . The appearance of Ti^0 in the fully-discharged electrode is in good agreement with what observed in HRTEM image and SAED pattern (Fig. 6a and 6b), together supporting the conversion reactions in TiP_2O_7 for Na storage.

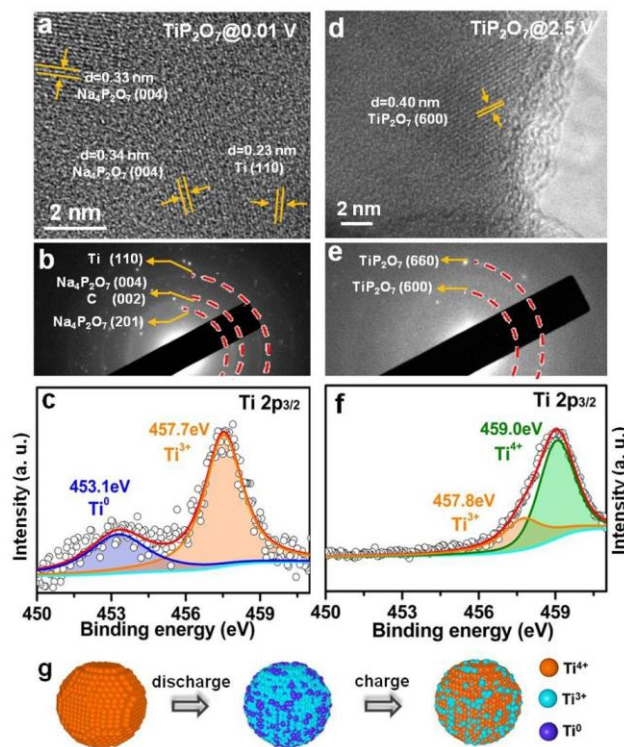
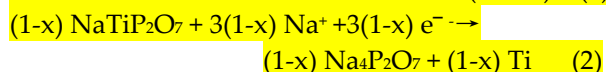
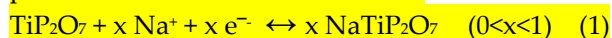


Figure 6 HRTEM images, SAED patterns, and XPS spectra (Ti 2p) of the electrode discharged to 0.01 V (a-c) or charged to 2.5 V (d-f). (g) Schematic illustration on the electrochemical reactions happened to TiP_2O_7 for reversible Na storage.

After the electrode is charged to 2.5 V, the XPS spectrum of Ti 2p is fitted by two peaks, *i. e.* one at 459.0 eV from Ti^{4+} and the other at 457.8 eV from Ti^{3+} (Fig. 6f). Their contents are 68.3% and 31.7% respectively.

The carefully check on these data leads to the following conclusions (Fig. 6g). 1) The conversion reaction between Ti^{3+} and Ti^0 is highly reversible, as supported by the disappearance of Ti^0 in the fully-charged electrode. This result is different from the case of TiO_2 , where the conversion reaction between Ti^{3+} and Ti^0 is almost irreversible [49]. This result will greatly affect the coulombic efficiency of TiO_2 . 2) The oxidation of Ti^0 likely stops at a stage of Ti^{3+} in the charge process, because the content of Ti^{3+} in the fully-charged electrode is very close to that of Ti^0 in the fully-discharged electrode. The obstacle to the further oxidation may arise from the local structure changes during the formation of Ti^0 , which greatly affect the local atom arrangements and the electronic structure. Therefore, the recovery from Ti^0

to Ti^{4+} is suppressed. If that's the case, the Ti^{3+} species that does not undergo the in-depth reduction to Ti^0 , basically remain the local structure, facilitating the oxidization of Ti^{3+} back to Ti^{4+} . This deduction is validated by the close quantity of Ti^{4+} in the fully-charged electrode and Ti^{3+} in the fully-discharged electrode, indirectly confirming our conclusion again. So, in other words, active Ti species participate only one of the redox reactions, either $\text{Ti}^{4+}/\text{Ti}^{3+}$ or $\text{Ti}^{3+}/\text{Ti}^0$. 3) Associated these redox reactions with the voltage profiles, it is believed that the intercalation reaction of $\text{Ti}^{4+}/\text{Ti}^{3+}$ occurs in high voltage (~ 1.8 V) and the conversion reaction of $\text{Ti}^{3+}/\text{Ti}^0$ happens in low voltage (~ 0.5 V). The two reactions may be overlapped in the middle, due to inevitable electrode overpotentials. 4) The reversible Na storage from the redox reactions of $\text{Ti}^{3+}/\text{Ti}^0$ and $\text{Ti}^{4+}/\text{Ti}^{3+}$ is ~ 0.91 Na and ~ 0.68 Na per formula. Although the data are roughly estimated based on Ti 2p, it indicates that the capacity contribution from $\text{Ti}^{3+}/\text{Ti}^0$ cannot be ignored. The quantity of Ti species that participates this redox reaction, may be not large, but the three-electron feature of this reaction still makes its contribution considerable. So, electrochemical reactions in the charge/discharge processes of TiP_2O_7 are as follows.



4 Conclusion

In summary, the electrochemical reactions of TiP_2O_7 as an anode material for NIBs are identified by *in-situ/ex-situ* techniques, where Ti^{3+} and Ti^0 appeared in the fully-discharged electrode along with the gradual fade-out of crystalline feature. It indicates that the conversion reaction is involved in the in-depth reduction. However, Ti^0 does not go back to Ti^{4+} in the fully-charged electrode, but suspends to Ti^{3+} , probably due to the irreversible local structure changes related to the in-depth reduction. In spite of this, the redox reaction between Ti^{3+} and Ti^0 is highly reversible, totally different from the reported case of TiO_2 . The three-electron feature of this redox reaction makes it significant contribution to the capacity, thus leading to the superior specific capacity of TiP_2O_7 even if there is a large "dead" mass of $\text{P}_2\text{O}_7^{4-}$. Meanwhile, the good stability of the discharge/charge products of TiP_2O_7 enhances the coulombic

efficiency upon cycling, similar to the case of $\text{NaTi}_2(\text{PO}_4)_3$. Therefore, TiP_2O_7 , which combines the benefits of TiO_2 and $\text{NaTi}_2(\text{PO}_4)_3$ together, can be regarded as a promising Ti-based anode material. Thus, $\text{TiP}_2\text{O}_7@\text{C}$ microflowers present the excellent electrochemical performances. Even after 10000 cycles at 2 A g^{-1} , there is still a capacity of 109 mAh g^{-1} , corresponding to a retention of 88%.

Acknowledgements

The authors are grateful for their financial support from the National Natural Science Foundation of China (Nos. 21971146, 61527809, and 21471090), Development Programs of Shandong Province (2017 GGX40101, 2017CXGC0503), Taishan Scholarship of Shandong Province (No. ts201511004), the Science, Technology and Innovation Commission of Shenzhen Municipality (JCYJ20180305164424922), and the Fundamental Research Funds of Shandong University (2018JC023). We thank Dr. Kepeng Song for high-resolution transmission electron microscope images and thank Dr. Tania Silver for helpful discussions.

Electronic Supplementary Material: Supplementary material (XRD pattern and SEM image of $\text{Ti}(\text{HPO}_4)_2$; EDS spectrum of $\text{TiP}_2\text{O}_7@\text{C}$; SAED pattern of $\text{TiP}_2\text{O}_7@\text{C}$; N_2 sorption isotherms of $\text{TiP}_2\text{O}_7@\text{C}$; XRD patterns, EDS spectra, and SEM images of TiO_2 , TiP_2O_7 and $\text{NaTi}_2(\text{PO}_4)_3$; Discharge/charge voltage profiles of TiO_2 , TiP_2O_7 and $\text{NaTi}_2(\text{PO}_4)_3$ at the first cycle; Voltage vs. Na number stored per formula of TiO_2 and TiP_2O_7 ; TEM image and SEM image of $\text{TiP}_2\text{O}_7@\text{C}$ after 10000 cycles; Discharge/charge profiles of $\text{TiP}_2\text{O}_7@\text{C}$ at a current density of 2.0 A g^{-1} ; EIS of TiP_2O_7 and $\text{TiP}_2\text{O}_7@\text{C}$ at 0.01 V ; The equivalent circuits; The sodium-storage properties of the reported Ti-based anodes; Interfacial impedances of TiP_2O_7 and $\text{TiP}_2\text{O}_7@\text{C}$ at 0.01 V ; *Ex-situ* XPS spectra of P 2p in TiP_2O_7 at different states of charge; *Ex-situ* XPS spectra of O 1s in TiP_2O_7 at different states of charge is available in the online version of this article at http://dx.doi.org/10.1007/s12274-***_****_*

References

- [1] Matthew, L.; Jun, L.; Chen, Z. W.; Amine, K. 30 years of lithium-ion batteries. *Adv. Mater.* **2018**, *30*, 1800561.
- [2] Assat, G.; Tarascon, J. M. Fundamental understanding and practical challenges of anionic redox activity in Li-ion batteries. *Nature Energy*, **2018**, *3*, 373-386.
- [3] Li, L.; Zheng, Y.; Zhang, S. L.; Yang, J. P.; Shao, Z. P.; Guo, Z. P. Recent progress on sodium ion batteries: potential high-performance anodes. *Energy Environ. Sci.* **2018**, *11*, 2310-2340.
- [4] Zhang, N.; Liu, Y. C.; Lu, Y. Y.; Han, X. P.; Cheng, F. Y.; Chen, J. Spherical nano-Sb@C composite as a high-rate and ultra-stable anode material for sodium-ion batteries. *Nano Res.* **2015**, *8*, 3384-3393.
- [5] Hwang, J. Y.; Myung, S. T.; Sun, Y. K. Sodium-ion batteries: present and future. *Chem. Soc. Rev.* **2017**, *46*, 3529-3614.
- [6] Pan, J.; Wang, N. N.; Zhou, Y. L.; Yang, X. F.; Zhou, W. Y.; Qian, Y. T.; Yang, J. Simple synthesis of a porous Sb/Sb₂O₃ nanocomposite for a high-capacity anode material in Na-ion batteries. *Nano Res.* **2017**, *10*, 1794-1803.
- [7] Hou, H. S.; Qiu, X. Q.; Wei, W. F.; Zhang, Y.; Ji, X. B. Carbon anode materials for advanced sodium-ion batteries. *Adv. Energy Mater.* **2017**, *7*, 1602898.
- [8] Xiao, L. F.; Cao, Y. L.; Henderson, W. A.; Sushko, M. L.; Shao, Y. Y.; Xiao, J.; Wang, W.; Engelhard, M. H.; Nie, Z. M.; Liu, J. Hard carbon nanoparticles as high-capacity, high-stability anodic materials for Na-ion batteries. *Nano Energy* **2016**, *19*, 279-288.
- [9] Wu, C. J.; Hua, W. B.; Zhang, Z.; Zhong, B. H.; Yang, Z. G.; Feng, G. L.; Xiang, W.; Wu, Z. G.; Guo, X. D. Design and synthesis of layered Na₂Ti₃O₇ and tunnel Na₂Ti₆O₁₃ hybrid structures with enhanced electrochemical behavior for sodium-ion batteries. *Adv. Sci.* **2018**, *5*, 1800519.
- [10] Liu, Y.; Liu, J. Y.; Hou, M. Y.; Fan, L.; Wang, Y. G.; Xia, Y. Y. Carbon-coated Li₄Ti₅O₁₂ Nanoparticles with high electrochemical performance as anode material in sodium-ion batteries. *J. Mater. Chem. A* **2017**, *5*, 10902-10908.
- [11] Wahid, M.; Puthusseri, D.; Gawli, Y.; Sharma, N.; Ogale, S. Hard carbons for sodium-ion battery anodes: synthetic strategies, material properties and storage mechanisms. *ChemSusChem* **2018**, *11*, 506-526.
- [12] Saurel, D.; Orayech, B.; Xiao, B. W.; Carriazo, D.; Li, X. L.; Rojo, T. From charge storage mechanism to performance: a roadmap toward high specific energy sodium ion batteries through carbon anode optimization. *Adv. Energy Mater.* **2018**, *8*, 1703268.
- [13] Senguttuvan, P.; Rousse, G.; Seznec, V. Tarascon, J. M.; Palacin, M. R. Na₂Ti₃O₇: lowest voltage ever reported oxide insertion electrode for sodium ion batteries. *Chem. Mater.* **2011**, *23*, 4109-4111.
- [14] Nie, S.; Liu, L.; Li, M.; Liu, J. F.; Xia, J.; Zhang, Y.; Wang, X. Y. Na₂Ti₃O₇/C nanofibers for high-rate and ultralong-life anodes in sodium-ion batteries. *ChemElectroChem* **2018**, *5*, 3498-3505.
- [15] Fang, Y. J.; Xiao, L. F.; Qian, J. F.; Cao, Y. L.; Ai, X. P.; Huang, Y. H.; Yang, H. X. 3D graphene decorated NaTi₂(PO₄)₃ microspheres as a superior high-rate and ultracycle-stable anode material for sodium ion batteries. *Adv. Energy Mater.* **2016**, *6*, 1502197.
- [16] Su, D.; Dou, S. X.; Wang, G. X. Anatase TiO₂: better anode material than amorphous and rutile phases of TiO₂ for Na-ion batteries. *Chem. Mater.* **2015**, *27*, 6022-6029.
- [17] Wang, D. X.; Liu, Q.; Chen, C. J.; Li, M. L.; Meng, X.; Bie, X. F. Wei, Y. J.; Huang, Y. H.; Du, F.; Wang, C. Z.; Chen, G. NASICON-structured NaTi₂(PO₄)₃@C nanocomposite as the low operation-voltage anode material for high-performance sodium-ion batteries. *ACS Appl. Mater. Interface* **2016**, *8*, 2238-2246.
- [18] Zhao, H. Y.; Zhang, F.; Zhang, S. M.; He, S. N.; Shen, F.; Han, X. G.; Yin, Y. D.; Cao, C. B. Scalable synthesis of sub-100 nm hollow carbon nanospheres for energy storage applications. *Nano Res.* **2018**, *11*, 1822-1833.
- [19] Song, T. B.; Chen, H.; Li, Z.; Xu, Q. J.; Liu, H. M.; Wang, Y. G.; Xia, Y. Y. Creating an air-stable sulfur-doped black phosphorus-TiO₂ composite as high-performance anode material for sodium-ion storage. *Adv. Funct. Mater.* **2019**, *29*, 1900535.
- [20] Le, Z. Y.; Liu, F.; Nie, P.; Li, X. R.; Liu, X. Y.; Bian, Z. F.; Chen, G.; Wu, H. B.; Lu, Y. F. Pseudocapacitive sodium storage in mesoporous single-crystal-like TiO₂-graphene nanocomposite enables high-performance sodium-ion capacitors. *ACS Nano* **2017**, *11*, 2952-2960.
- [21] Guo, X.; Zhang, J. Q.; Song, J. J.; Wu, W. J.; Liu, H.; Wang, G. X. MXene encapsulated titanium oxide nanospheres for ultra-stable and fast sodium storage. *Energy Storage Materials* **2018**, *14*, 306-313.
- [22] Li, K. K.; Zhang, J.; Lin, D. M.; Wang, D. W.; Li, B. H.; Lv, W.; Sun, S.; He, Y. B.; Kang, F. Y.; Yang, Q. H.; Zhou, L. M.; Zhang, T. Y. Evolution of the electrochemical interface in sodium ion batteries with ether electrolytes. *Nat. Commun.* **2019**, *10*, 1248.
- [23] Wu, L. M.; Bresser, D.; Buchholz, D.; Giffin, G. A.; Castro, C. R.; Ochel, A.; Passerini, S. Unfolding the mechanism of sodium insertion in anatase TiO₂ nanoparticles. *Adv. Energy Mater.* **2015**, *5*, 1401142.
- [24] Longoni, G.; Cabrera, R. L. P.; Polizzi, S.; Arienzo, M. D.; Mari, C. M.; Cui, Y.; Ruffo, R. Shape-controlled TiO₂ nanocrystals for Na-ion battery electrodes: the role of different exposed crystal facets on the electrochemical properties. *Nano Lett.* **2017**, *17*, 992-1000.
- [25] Sanz, J.; Iglesias, J. E. Structural Disorder in the cubic 3 × 3 × 3 superstructure of TiP₂O₇. XRD and NMR study. *Chem. Mater.* **1997**, *9*, 996-1003.
- [26] Kim, K. T.; Ali, G.; Chung, K. Y.; Yoon, C. S.; Yashiro, H. S.; Sun, Y. K.; Lu, J.; Amine, K.; Myung, S. T. Anatase titania nanorods as an intercalation anode material for

- rechargeable sodium batteries, *Nano Lett.* **2014**, *14*, 416-422.
- [27] Pan, J.; Chen, S. L.; Zhang, D. P.; Xu, X. N.; Sun, Y. W.; Tian, F.; Gao, P.; Yang, J. SnP₂O₇ covered carbon nanosheets as a long-life and high-rate anode material for sodium-ion batteries. *Adv. Funct. Mater.* **2018**, *28*, 1804672.
- [28] Pan, J.; Chen, S. L.; Fu, Q.; Sun, Y. W.; Zhang, Y. C.; Lin, N.; Gao, P.; Yang, J.; Qian, Y. T. Layered-structure SbPO₄/reduced graphene oxide: an advanced anode material for sodium ion batteries. *ACS Nano* **2018**, *12*, 12869-12878.
- [29] Pan, J.; Zhang, Y. C.; Li, L. L.; Cheng, Z. J.; Li, Y. L.; Yang, X. F.; Yang, J.; Qian, Y. T. Polyanions enhance conversion reactions for lithium/sodium-ion batteries: the case of SbVO₄ nanoparticles on reduced graphene oxide. *Small Methods* **2019**, *3*, 1900231.
- [30] Senguttuvan, P.; Rouse, G.; Oro-Sole, J.; Tarascon, J. M.; Palacin, M. R. A low temperature TiP₂O₇ polymorph exhibiting reversible insertion of lithium and sodium ions. *J. Mater. Chem. A* **2013**, *1*, 15284-15291.
- [31] Hu, Q.; Liang, J.; Liao, J.; Tang, Z.; Ding, X.; Chen, C. H. A comparative study on nanocrystalline layered and crystalline cubic TiP₂O₇ for rechargeable Li/Na/K alkali metal batteries. *J. Mater. Chem. A* **2018**, *6*, 15230-15236.
- [32] Li, Z. T.; Dong, Y. F.; Feng, J. Z.; Xu, T.; Ren, H.; Gao, C.; Li, Y. R.; Cheng, M. J.; Wu, W. T.; Wu, M. B. Controllably enriched oxygen vacancies through polymer assistance in titanium pyrophosphate as a super anode for Na/K-ion batteries. *ACS Nano* **2019**, *13*, 9227-9236.
- [33] Wen, Y.; Chen, L.; Pang, Y.; Guo, Z.; Bin, D.; Wang, Y.; Wang, C.; Xia, Y. TiP₂O₇ and expanded graphite nanocomposites as anode material for aqueous lithium-ion batteries. *ACS Appl. Mater. Interfaces* **2017**, *9*, 8075-8082.
- [34] Yee, G.; Shanbhag, S.; Wu, W.; Carlisle, K.; Chang, J.; Whitacre, J. F. TiP₂O₇ exhibiting reversible interaction with sodium ions in aqueous electrolytes. *Electrochem. Commun.* **2018**, *86*, 104-107.
- [35] Chu, C. X.; Yang, J.; Zhang, Q. Q.; Wang, N. N.; Niu, F. E.; Xu, X. N.; Yang, J.; Fan, W. L.; Qian, Y. T. Biphasic-interface enhanced sodium storage and accelerated charge transfer: flower-like anatase/bronze TiO₂/C as an advanced anode material for Na-ion batteries. *ACS Appl. Mater. Interfaces* **2017**, *9*, 43648-43656.
- [36] Sun, Y. R.; Gai, L. G.; Zhou, Y.; Zuo, X. Z.; Zhou, J. H.; Jiang, H. H. Polyhierarchically structured TiP₂O₇/C microparticles with enhanced electrochemical performance for lithium-ion batteries. *CrystEngComm* **2014**, *16*, 10681-10691.
- [37] Xu, C.; Xu, Y. N.; Tang, C. J.; Wei, Q. L.; Meng, J. S.; Huang, L.; Zhou, L.; Zhang, G. B.; He, L.; Mai, L. Q. Carbon-coated hierarchical NaTi₂(PO₄)₃ mesoporous microflowers with superior sodium storage performance. *Nano Energy* **2016**, *28*, 224-231.
- [38] Xing, O.; Yang, C. H.; Xiong, X. H.; Zheng, F. H.; Pan, Q. C.; Jin, C.; Liu, M. L.; Huang, K. A new rGO-overcoated Sb₂Se₃ nanorods anode for Na⁺ battery: in situ X-ray diffraction study on a live sodiation/desodiation process. *Adv. Funct. Mater.* **2017**, *27*, 1606242.
- [39] Wei, Z. X.; Wang, D. X.; Li, M. L.; Guo, Y.; Wang, C. Z.; Chen, G.; Du, F. Fabrication of hierarchical potassium titanium phosphate spheroids: a host material for sodium-ion and potassium-ion storage. *Adv. Energy Mater.* **2018**, *8*, 1801102.
- [40] Li, L.; Seng, K. H.; Li, D.; Xia, Y. Y.; Liu, H. K.; Guo, Z. P. SnSb@carbon nanocable anchored on graphene sheets for sodium ion batteries. *Nano Res.* **2014**, *7*, 1466-1476.
- [41] Xu, Z. L.; Lim, K.; Park, K. Y.; Yoon, G.; Seong, W. M.; Kang, K. Engineering solid electrolyte interphase for pseudocapacitive anatase TiO₂ anodes in sodium-ion batteries. *Adv. Funct. Mater.* **2018**, *28*, 1802099.
- [42] Wang, N. N.; Bai, Z. C.; Qian, Y. T.; Yang, J. One-dimensional yolk-shell Sb@Ti-O-P nanostructures as a high-capacity and high-rate anode material for sodium ion batteries. *ACS Appl. Mater. Interface* **2017**, *9*, 447-454.
- [43] Zeng, C.; Xie, F. X.; Yang, X. F.; Jaronec, M.; Zhang, L.; Qiao, S. Z. Ultrathin titanate nanosheets/graphene films derived from confined transformation for excellent Na/K ion storage. *Angew. Chem. Int. Ed.* **2018**, *57*, 8540-8544.
- [44] Chao, D. L.; Zhu, C. R.; Yang, P. H.; Xia, X. H.; Liu, J. L.; Wang, J.; Fan, X. F.; Savilov, S. V.; Lin, J. Y.; Fan, H. J.; Shen, Z. X. Array of nanosheets render ultrafast and high-capacity na-ion storage by tunable pseudocapacitance. *Nat. Commun.* **2016**, *7*, 12122.
- [45] Wu, C.; Kopold, P.; Ding, Y. L.; Aken, P. A. V.; Maier, J.; Yu, Y. Synthesizing porous NaTi₂(PO₄)₃ nanoparticles embedded in 3D graphene networks for high-rate and long cycle-life sodium electrodes. *ACS Nano* **2015**, *9*, 6610-6618.
- [46] Yang, G. Z.; Song, H. W.; Wu, M. M.; Wang, C. X.; Porous NaTi₂(PO₄)₃ nanocubes: a high-rate nonaqueous sodium anode material with more than 10000 cycle life. *J. Mater. Chem. A* **2015**, *3*, 18718-18726.
- [47] Augustyn, V.; Come, J.; Lowe, M. A.; Kim, J. W.; Taberna, P. L.; Tolbert, S. H.; Abruna, H. D.; Simon, P.; Dunn, B. High-rate electrochemical energy storage through Li^C intercalation pseudocapacitance. *Nat. Mater.* **2013**, *12*, 518-522.
- [48] Brezesinski, T.; Wang, J.; Polleux, J.; Dunn, B.; Tolbert, S. H. Templated nanocrystal-based porous TiO₂ films for next-generation electrochemical capacitors. *J. Am. Chem. Soc.* **2009**, *131*, 1802-1809.
- [49] Hwang, J. Y.; Du, H. L.; Yun, B. N.; Jeong, M. G.; Kim, J. S.; Kim, H.; Jung, H. G.; Sun, Y. K. Carbon-free TiO₂ microspheres as anode materials for sodium ion batteries. *ACS Energy Lett.* **2019**, *4*, 494-501.

Electronic Supplementary Material

Improved Na Storage and Coulombic Efficiency in $\text{TiP}_2\text{O}_7@C$ Microflowers for Sodium Ion Batteries

Jun Pan^{1,2}, Nana Wang³, Lili Li⁴, Feng Zhang¹, Zhenjie Cheng¹, Yanlu Li⁴, Jian Yang,^{*1,2} (✉) and Yitai Qian¹

¹ Key Laboratory of Colloid and Interface Chemistry, Ministry of Education, School of Chemistry and Chemical Engineering Shandong University, Jinan 250100, P. R. China.

² Shenzhen Research Institute of Shandong University, Shenzhen 518000, P. R. China.

³ Institute for Superconducting and Electronic Materials, Australian Institute for Innovative Materials, University of Wollongong Innovation Campus, North Wollongong New South Wales 2500, Australia.

⁴ State Key Lab of Crystal Materials, Shandong University, Jinan 250100, P. R. China.

Supporting information to DOI 10.1007/s12274-****-****-* (automatically inserted by the publisher)

Figure Captions

- Figure S1** (a) XRD pattern and (b) SEM image of $\text{Ti}(\text{HPO}_4)_2$.
- Figure S2** EDS spectrum of $\text{TiP}_2\text{O}_7@\text{C}$.
- Figure S3** SAED pattern of $\text{TiP}_2\text{O}_7@\text{C}$.
- Figure S4** N_2 sorption isotherms of $\text{TiP}_2\text{O}_7@\text{C}$.
- Figure S5** XRD patterns of (a) TiO_2 , (b) TiP_2O_7 , (c) $\text{NaTi}_2(\text{PO}_4)_3$.
- Figure S6** EDS spectra of (a) TiO_2 , (b) TiP_2O_7 , (c) $\text{NaTi}_2(\text{PO}_4)_3$.
- Figure S7** SEM images of (a) TiO_2 , (b) TiP_2O_7 , (c) $\text{NaTi}_2(\text{PO}_4)_3$.
- Figure S8** Discharge/charge voltage profiles of (a) TiO_2 , (b) TiP_2O_7 and (c) $\text{NaTi}_2(\text{PO}_4)_3$ at the first cycle.
- Figure S9** Voltage *vs.* Na number stored per formula of TiO_2 and TiP_2O_7 .
- Figure S10** (a) TEM image and (b) SEM image of $\text{TiP}_2\text{O}_7@\text{C}$ after 10000 cycles.
- Figure S11** (a) EIS of TiP_2O_7 and $\text{TiP}_2\text{O}_7@\text{C}$ at D0.01 V. (b) The equivalent circuits.
- Figure S12** *Ex-situ* XPS spectra of P 2p in TiP_2O_7 at different states of charge. (a) D 0.01 V, (b) C 2.5 V.
- Figure S13** *Ex-situ* XPS spectra of O1s in TiP_2O_7 at different states of charge. (a) D 0.01 V. (b) C 2.5 V.

Table Captions

- Table S1** The sodium-storage properties of the reported Ti-based anodes.
- Table S2** Interfacial Impedances of TiP_2O_7 and $\text{TiP}_2\text{O}_7@\text{C}$ at 0.01 V.

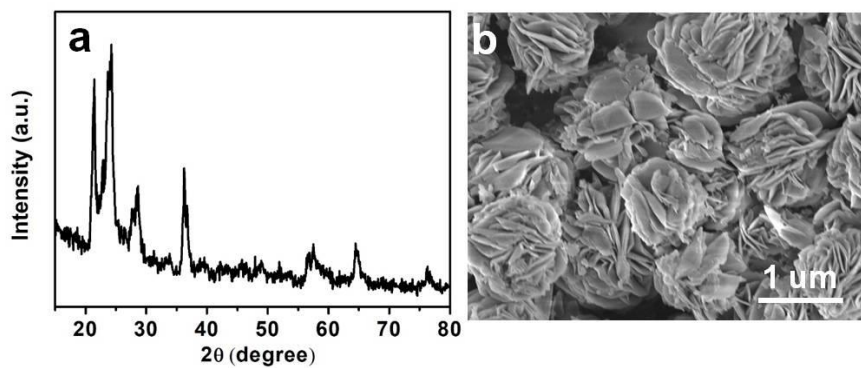


Figure S1 (a) XRD pattern and (b) SEM image of $\text{Ti}(\text{HPO}_4)_2$.

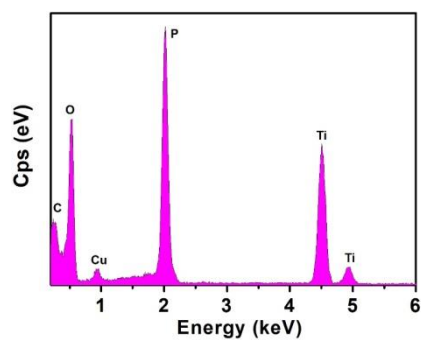


Figure S2 EDS spectrum of $\text{TiP}_2\text{O}_7@\text{C}$.

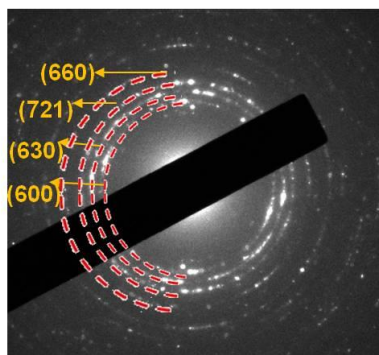


Figure S3 SAED pattern of $\text{TiP}_2\text{O}_7@\text{C}$.

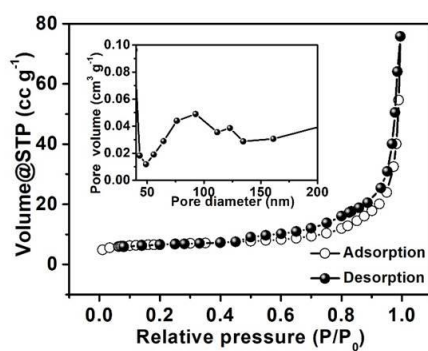


Figure S4 N₂ sorption isotherms of TiP₂O₇@C.

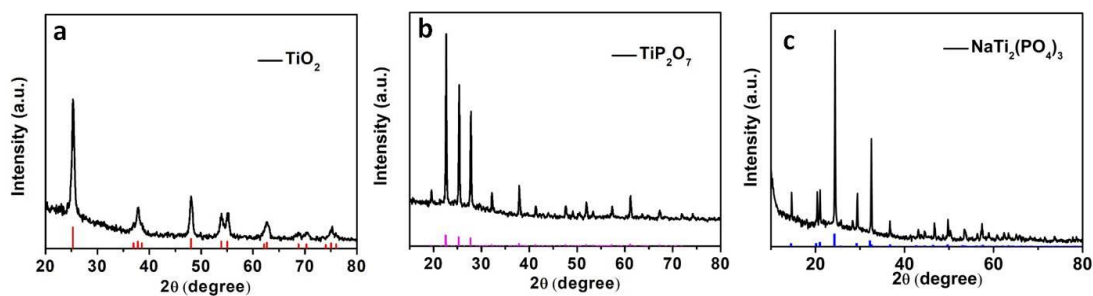


Figure S5 XRD patterns of (a) TiO₂, (b) TiP₂O₇, (c) NaTi₂(PO₄)₃.

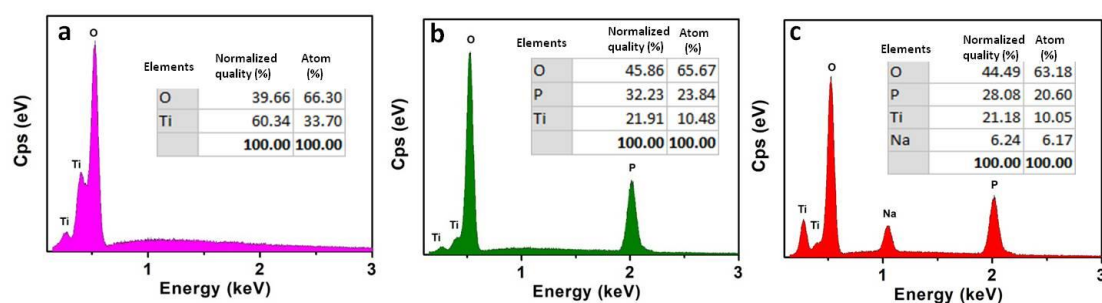


Figure S6 EDS spectra of (a) TiO₂, (b) TiP₂O₇, (c) NaTi₂(PO₄)₃.

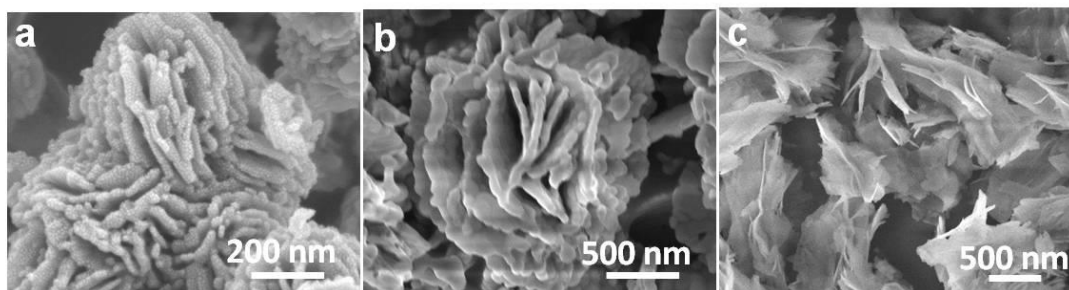


Figure S7 SEM images of (a) TiO_2 , (b) TiP_2O_7 , (c) $\text{NaTi}_2(\text{PO}_4)_3$.

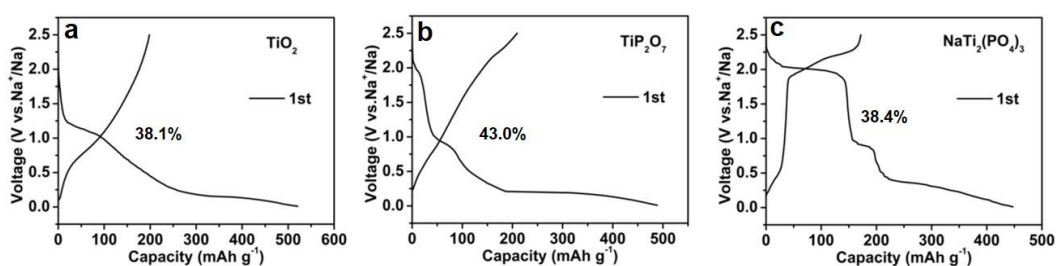


Figure S8 Discharge/charge voltage profiles of (a) TiO_2 , (b) TiP_2O_7 and (c) $\text{NaTi}_2(\text{PO}_4)_3$ at the first cycle.

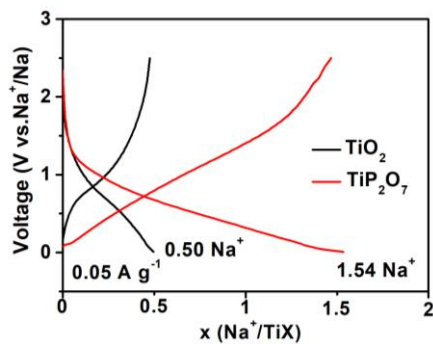


Figure S9 Voltage *vs.* Na number stored per formula of TiO_2 and TiP_2O_7 .

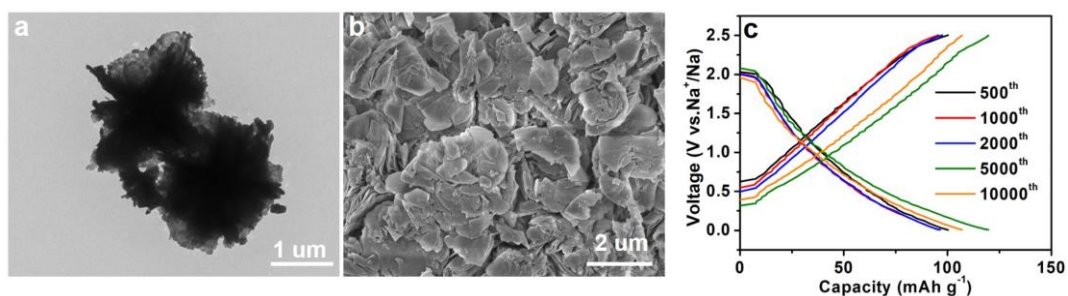


Figure S10 (a) TEM image and (b) SEM image of $\text{TiP}_2\text{O}_7@\text{C}$ after 10000 cycles. (c) Discharge/charge profiles of $\text{TiP}_2\text{O}_7@\text{C}$ at a current density of 2.0 A g^{-1} .

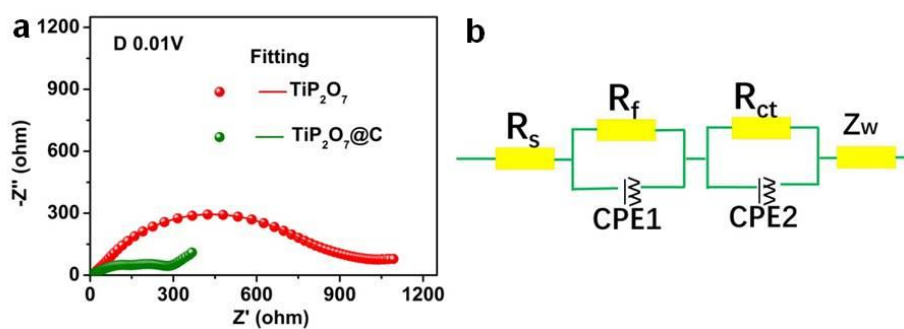


Figure S11 (a) EIS of TiP_2O_7 and $\text{TiP}_2\text{O}_7@\text{C}$ at D0.01 V. (b) The equivalent circuits.

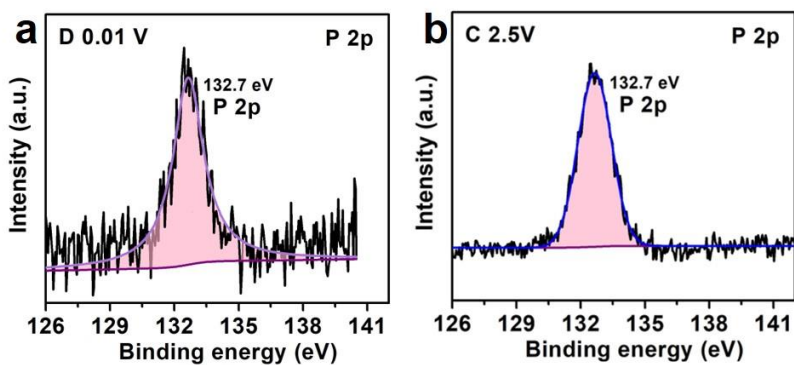


Figure S12 *Ex-situ* XPS spectra of P 2p in TiP_2O_7 at different states of charge. (a) D 0.01 V, (b) C 2.5 V.

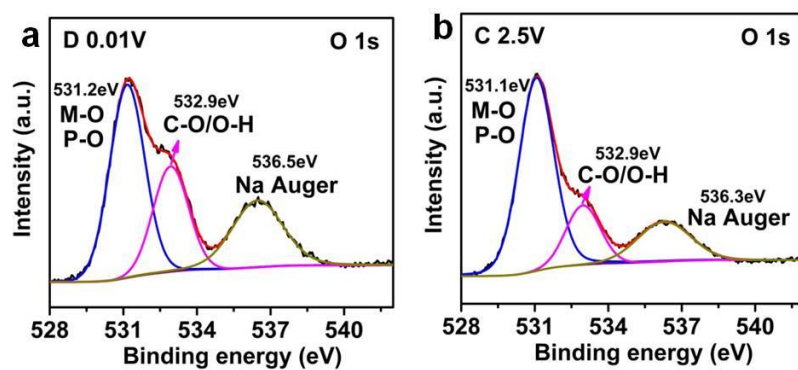


Figure S13 *Ex-situ* XPS spectra of O1s in TiP_2O_7 at different states of charge. (a) Initial. (b) D 0.01 V. (c) C 2.5 V.

Table S1 The sodium-storage properties of the reported Ti-based anodes.

Ti-based anode	Capacity [mA h g ⁻¹]	Cycle life	Capacity retention [%]	Ref.
B-TiO ₂ (B)-P	90.2 at 10 A g ⁻¹	5000	86	1
Branched TiO ₂ /C	283.5 at 0.2 A g ⁻¹	1000	86.1	2
TiO ₂ -BP-S	290 at 0.3 A g ⁻¹	300	72.5	3
P-modulated TiO ₂	190 at 10 A g ⁻¹	5000	93	4
TiO ₂ (A/B)-MS	125 at 3.35 A g ⁻¹	1000	100	5
TiO ₂ SNTs	107.4 at 5A g ⁻¹	4000	82.2	6
OVs-TiO _{2-x}	125 at 2 A g ⁻¹	3600	78	7
TiO ₂ @Ti ₃ C ₂ T _x	102 at 0.96 A g ⁻¹	5000	97.1	8
TiO ₂	136 at 2 A g ⁻¹	600	89	9
CNS-S@TiO ₂	215 at 2 A g ⁻¹	1000	69.4	10
R-TiO _{2-x} -S	128.5 at 10 A g ⁻¹	6500	100	11
P-TiO ₂	141 at 3.35 A g ⁻¹	1000	94	12
TiO ₂ /C HRTs	153.9 at 3.35 A g ⁻¹	14000	100	13
TiO ₂ -G	90 at 3.35 A g ⁻¹	5000	100	14
TiO ₂ @CNT@C	165 at 1 A g ⁻¹	1000	93	15
B-TiO ₂ (B)	80.9 at 3.35 A g ⁻¹	5000	94.4	16
MWTOG	162 at 1.675 A g ⁻¹	7000	92.6	17
NC TiO ₂ -Y	90.6 at 8.35 A g ⁻¹	3000	95.5	18
TiO ₂	105 at 0.05 A g ⁻¹	600	100	19
IOam-TiO ₂	105 at 2 A g ⁻¹	500	52.5	20
G/P-RTiO ₂	144.5 at 3.35A g ⁻¹	4000	94.4	21
TiO ₂ /C	71 at 1 A g ⁻¹	500	100	22
S-TiO ₂	136 at 3.35 A g ⁻¹	4400	91	23
C-TiO ₂	180 at 1.675 A g ⁻¹	500	100	24
TiO ₂ @C	136 at 0.64 A g ⁻¹	500	90.6	25
TiO ₂ -F/CNTs	190 at 0.1 A g ⁻¹	100	97	26
G-TiO ₂	110 at 0.5 A g ⁻¹	4000	55	27
TiO ₂	155 at 0.033 A g ⁻¹	200	99.7	28
C-TiO ₂	91 at 1.65 A g ⁻¹	50	90.7	29
TiO ₂	165 at 0.1 A g ⁻¹	500	68.8	30
TiO ₂ ∩NPCS	152 at 0.67 A g ⁻¹	3000	100	31
TiO ₂ @NFG	162 at 0.67 A g ⁻¹	2200	90	32
TiP ₂ O ₇ @C	108 at 2 A g ⁻¹	10000	88	This work

References

- [1] Kang, M. L.; Ruan, Y. R.; Lu, Y. Z.; Luo, L.; Huang, J. X.; Zhang, J. M.; Hong, Z. S. An interlayer defect promoting the doping of the phosphate group into TiO₂(B) nanowires with unusual structure properties towards ultra-fast and ultra-stable sodium storage. *J. Mater. Chem. A* **2019**, *7*, 16937-16946.
- [2] Wang, L.; Yang, G. R.; Wang, J. N.; Wang, S. L.; Wang, C. Y.; Peng, S. J.; Yan, W.; Ramakrishna, S. In situ fabrication of branched TiO₂/C nanofibers as binder-free and free-standing anodes for high-performance sodium-ion batteries. *Small* **2019**, *15*, 1901584.
- [3] Song, T. B.; Chen, H.; Li, Z.; Xu, Q. J.; Liu, H. M.; Wang, Y. G.; Xia, Y. Y.; Creating an air-stable sulfur-doped black phosphorus-TiO₂ composite as high-performance anode material for sodium-ion storage. *Adv. Funct. Mater.* **2019**, *29*, 1900535.
- [4] Xia, Q. B.; Huang, Y.; Xiao, J.; Wang, L.; Lin, Z. H.; Li, W. J.; Liu, H.; Gu, Q. F.; Liu, H. K.; Chou, S. L. Phosphorus-modulation-triggered surface disorder in titanium dioxide nanocrystals enables exceptional sodium-storage performance. *Angew. Chem. Int. Ed.* **2019**, *58*, 4022-4026.
- [5] Hwang, J. Y.; Du, H. L.; Yun, B. N.; Jeong, M. G.; Kim, J. S.; Kim, H.; Jung, H. G.; Sun, Y. K. Carbon-free TiO₂ microspheres as anode materials for sodium ion batteries. *ACS Energy Lett.* **2019**, *4*, 494-501.
- [6] Chen, B.; Meng, T. H.; Xie, F. X.; He, F.; He, C. N.; Davey, K.; Zhao, N. Q.; Qiao, S. Z. 1D Sub-nanotubes with anatase/bronze TiO₂ nanocrystal wall for high-rate and long-life sodium-ion batteries. *Adv. Mater.* **2018**, *30*, 1804116.
- [7] Ma, L. B.; Gao, X.; Zhang, W. J.; Yuan, H.; Hu, Y.; Zhu, G. Y.; Chen, R. P.; Chen, T.; Tie, Z. X.; Liu, J.; Wu, T.; Jin, Z. Ultrahigh rate capability and ultralong cycling stability of sodium-ion batteries enabled by wrinkled black titania nanosheets with abundant oxygen vacancies. *Nano Energy* **2018**, *53*, 91-96.
- [8] Guo, X.; Zhang, J. Q.; Song, J. J.; Wu, W. J.; Liu, H.; Wang, G. X. MXene encapsulated titanium oxide nanospheres for ultra-stable and fast sodium storage. *Energy Storage Materials* **2018**, *14*, 306-313.
- [9] Xu, Z. L.; Lim, K.; Park, K. Y.; Yoon, G.; Seong, W. M.; Kang, K. Engineering solid electrolyte interphase for pseudocapacitive anatase TiO₂ anodes in sodium-ion batteries. *Adv. Funct. Mater.* **2018**, *28*, 1802099.
- [10] Chen, C. M.; Yang, Y. C.; Ding, S. S.; Wei, Z. X.; Tang, X.; Li, P. C.; Wang, T. H.; Cao, G. Z.; Zhang, M. S-doped carbon@TiO₂ to store Li⁺/Na⁺ with high capacity and long life-time. *Energy Storage Materials* **2018**, *13*, 215-222.
- [11] He, H. N.; Huang, D.; Pang, W. K.; Sun, D.; Wang, Q.; Tang, Y. G.; Ji, X. B.; Guo, Z. P.; Wang, H. Y. Plasma-induced amorphous shell and deep cation-site s doping endow TiO₂ with extraordinary sodium storage performance. *Adv. Mater.* **2018**, *30*, 1801013.
- [12] Ni, J. F.; Fu, S. D.; Yuan, Y. F.; Ma, L.; Liang, Y.; Li, L.; Lu, J. Boosting sodium storage in TiO₂ nanotube arrays through surface phosphorylation. *Adv. Mater.* **2018**, *30*, 1704337.
- [13] He, H. N.; Gan, Q. M.; Wang, H. Y.; Xu, G. L.; Zhang, X. Y.; Huang, D.; Fu, F.; Tang, Y. G.; Amine, K.; Shao, M. H. Structure-dependent performance of TiO₂/C as anode material for na-ion batteries. *Nano Energy* **2018**, *44*, 217-227.
- [14] Xu, G. L.; Xiao, L. S.; Sheng, T.; Liu, J. Z.; Hu, Y. X.; Ma, T. Y.; Amine, R.; Xie, Y. Y.; Zhang, X. Y.; Liu, Y. Z.; Ren, Y.; Sun, C. J.; Heald, S. M.; Kovacevic, J.; Sehlikeier, Y. H.; Schulz, C.; Mattis, W. J. L.; Sun, S. G.; Wiggers, H.; Chen, Z. H.; Amine, K. Electrostatic self-assembly enabling integrated bulk and interfacial sodium storage in 3D titania-graphene hybrid. *Nano Lett.* **2018**, *18*, 336-346.

- [15] Zhu, Y. E.; Yang, L. P.; Sheng, J.; Chen, Y. N.; Gu, H. C.; Wei, J. P.; Zhou, Z. Fast sodium storage in TiO₂@CNT@C nanorods for high-performance na-ion capacitors. *Adv. Energy Mater.* **2017**, *7*, 1701222.
- [16] Zhang, Y.; Ding, Z. Y.; Foster, C. W.; Banks, C. E.; Qiu, X. Q.; Ji, X. B. Oxygen vacancies evoked blue TiO₂(B) nanobelts with efficiency enhancement in sodium storage behaviors. *Adv. Funct. Mater.* **2017**, *27*, 1700856.
- [17] Le, Z. Y.; Liu, F.; Nie, P.; Li, X. R.; Liu, X. Y.; Bian, Z. F.; Chen, G.; Wu, H. B.; Lu, Y. F. Pseudocapacitive sodium storage in mesoporous single-crystal-like TiO₂-graphene nanocomposite enables high-performance sodium-ion capacitors. *ACS Nano* **2017**, *11*, 2952-2960.
- [18] Zhang, Y.; Wang, C. W.; Hou, H. S.; Zou, G. Q.; Ji, X. B. Nitrogen doped/carbon tuning yolk-like TiO₂ and its remarkable impact on sodium storage performances. *Adv. Energy Mater.* **2017**, *7*, 1600173.
- [19] Longoni, G.; Cabrera, R. L. P.; Polizzi, S.; Arienzo, M. D.; Mari, C. M.; Cui, Y.; Ruffo, R. Shape-controlled TiO₂ nanocrystals for na-ion battery electrodes: the role of different exposed crystal facets on the electrochemical properties. *Nano Lett.* **2017**, *17*, 992-1000.
- [20] Zhou, M.; Xu, Y.; Wang, C. L.; Li, Q. W.; Xiang, J. X.; Liang, L. Y.; Wu, M. H.; Zhao, H. P.; Lei, Y. Amorphous TiO₂ inverse opal anode for high-rate sodium ion batteries. *Nano Energy* **2017**, *31*, 514-524.
- [21] Zhang, Y.; Foster, C. W.; Banks, C. E.; Shao, L. D.; Hou, H. S.; Zou, G. Q.; Chen, J.; Huang, Z. D.; Ji, X. B. Graphene-rich wrapped petal-like rutile TiO₂ tuned by carbon dots for high-performance sodium storage. *Adv. Mater.* **2016**, *28*, 9391-9399.
- [22] Wang, N.; Gao, Y.; Wang, Y. X.; Liu, K.; Lai, W. H.; Hu, Y. M.; Zhao, Y.; Chou, S. L.; Jiang, L. Nanoengineering to achieve high sodium storage: a case study of carbon coated hierarchical nanoporous TiO₂ microfibers. *Adv. Sci.* **2016**, *3*, 1600013.
- [23] Ni, J. F.; Fu, S. D.; Wu, C.; Maier, J.; Yu, Y.; Li, L. Self-supported Nanotube arrays of sulfur-doped TiO₂ enabling ultrastable and robust sodium storage. *Adv. Mater.* **2016**, *28*, 2259-2265.
- [24] Tahir, M. N.; Oschmann, B.; Buchholz, D.; Dou, X. W.; Lieberwirth, I.; Panthofer, M.; Tremel, W.; Zentel, R.; Passerini, S. Extraordinary performance of carbon-coated anatase TiO₂ as sodium-ion anode. *Adv. Energy Mater.* **2016**, *6*, 1501489.
- [25] Su, D.; Dou, S. X.; Wang, G. X. Anatase TiO₂: better anode material than amorphous and rutile phases of TiO₂ for Na-ion batteries. *Chem. Mater.* **2015**, *27*, 6022-6029.
- [26] Huang, J. Y.; Myung, S. T.; Lee, J. H.; Abouimrane, A.; Belharouak, I.; Sun, Y. K. Ultrafast sodium storage in anatase TiO₂ nanoparticles embedded on carbon nanotubes. *Nano Energy* **2015**, *16*, 218-226.
- [27] Chen, C. J.; Wen, Y. W.; Hu, X. L.; Ji, X. L.; Yan, M. Y.; Mai, L. Q.; Hu, P.; Shan, B.; Huang, Y. H. Na⁺ Intercalation pseudocapacitance in graphene-coupled titanium oxide enabling ultra-fast sodium storage and long-term cycling. *Nat. Commun.* **2015**, *6*, 6929.
- [28] Wu, L. M.; Bresser, D.; Buchholz, D.; Giffin, G. A.; Castro, C. R.; Ochel, A.; Passerini, S. Unfolding the mechanism of sodium insertion in anatase TiO₂ nanoparticles. *Adv. Energy Mater.* **2015**, *5*, 1401142.
- [29] Kim, K. T.; Ali, G.; Chung, K. Y.; Yoon, C. S.; Yashiro, H. S.; Sun, Y. K.; Lu, J.; Amine, K.; Myung, S. T. Anatase titania nanorods as an intercalation anode material for rechargeable sodium batteries. *Nano Lett.* **2014**, *14*, 416-422.
- [30] Li, K. K.; Zhang, J.; Lin, D. M.; Wang, D. W.; Li, B. H.; Lv, W.; Sun, S.; He, Y. B.; Kang, F. Y.; Yang, Q. H.; Zhou, L. M.; Zhang, T. Y. Evolution of the electrochemical interface in sodium ion batteries with ether electrolytes. *Nat. Commun.* **2019**, *10*, 1248.

- [31] Li, B. S.; Xi, B. J.; Wu, F. F.; Mao, H. Z.; Liu, J.; Feng, J. K.; Xiong, S. L. One-step in Situ formation of n-doped carbon nanosheet 3d porous networks/TiO₂ hybrids with ultrafast sodium storage. *Adv. Energy Mater.* **2019**, *9*, 1803070.
- [32] Li, B. S.; Xi, B. J.; Feng, Z. Y.; Lin, Y.; Liu, J. C.; Feng, J. K.; Qian, Y. T.; Xiong, S. L. Hierarchical porous nanosheets constructed by graphene-coated, interconnected TiO₂ nanoparticles for ultrafast sodium storage. *Adv. Mater.* **2018**, *30*, 1705788.

Table S2 Interfacial Impedances of TiP₂O₇ and TiP₂O₇@C at 0.01 V.

1 st D 0.01 V			
ohm	R _s	R _f	R _{ct}
TiP ₂ O ₇	16.9	456	565
TiP ₂ O ₇ @C	13.6	54.7	234